Supplementary Material for "[Prospective Real-Time Slow Slip Events Forecasting"

Adriano Gualandi[1*], Matthieu Darcy[2] and Fabio Corbi[3]

[1*]Bullard Laboratories, Department of Earth Sciences, University of Cambridge, Madingley Rise, Madingley Road, Cambridge, CB3 0EZ, United Kingdom.
[2]Division of Engineering and Applied Science, Department of Computing and Mathematical Sciences, California Institute of Technology, 1200, E. California Blvd, Pasadena, 91125, CA, United States of America.
[3]Istituto di Geologia Ambientale e Geoingegneria – CNR, Dipartimento di Scienze della Terra,, Sapienza Università di Roma, Piazzale Aldo Moro, 5, Rome, 00185, Italy.

*Corresponding author(s). E-mail(s): ag2347@cam.ac.uk;

Introduction

Section S1 presents the data used in this study. It is subdivided into two subsection to cover both geodetic and seismic data.

Section S2 presents an automatic SSE detection algorithm, used to visualize the segmentation of the Cascadia subduction zone.

Section S3 offers a description of the physical intuition behind the modelling strategy.

Section S4 introduces the various forecasting models, both deterministic and probabilistic.

In section S5 we describe the evaluation metrics.

This files contains 5 Figures, 11 Tables, and the description of the Movie S1.

S1 Data

S1.1 Geodetic data

The geodetic input data is the slip potency with respect to the long-term loading (P) as described in [1]. Here we refer to it as slip potency, implying that it is the slip potency derived from detrended time series, i.e. referring to variations with respect to the long-term trend. For every patch j and time n, the slip potency P_{jn} is equal to $A_j\delta_{jn}$, where A_j is the slipping area for the patch j that slipped an amount δ_{jn} at time n with respect to the long-term value. Under the assumption of constant shear modulus μ, P_{jn} is proportional to the seismic moment associated with the patch j. The seismic moment is logarithmically related to the equivalent moment magnitude, and is a standard quantity to effectively measure the size of a slipping event [2, 3]. δ_{jn} is already the result of several processing assumptions, and it is derived from GNSS position time series. The most relevant information and assumptions are the following:

- The GNSS position time series from EarthScope (https://www.earthscope.org) include both final and rapid solutions, with data available up to 2 days before the current date.
- The time series are detrended and corrected for instrumental and co-seismic offsets. The removal of a linear trend implies that the displacements are relative to the long-term motion.
- The dataset is decomposed in independent components (ICs), and those relative to SSEs are automatically selected analyzing both their spatial distribution and the power spectrum of their time evolution. The number of ICs is automatically selected thanks to a variational Bayesian approach, and it can change from one day to the next depending on the input dataset.
- The spatial distribution of the selected ICs is inverted on a triangular mesh [4] using a half-space elastic solution [5] to find the corresponding pattern on the fault. The

regularization parameter is automatically selected via a leave-one-out procedure [6, 7].

- The spatial distributions on the fault are recombined with the corresponding temporal evolutions to retrieve the full slip spatio-temporal history.
- The slip spatio-temporal history is multiplied by the area of the slipping patches to obtain the slip potency spatio-temporal history.

The above procedure is repeated every day starting from 2024/08/01. This means that we have a collection of solutions from 2024/08/01 to two days ago, each giving a slip potency spatio-temporal matrix of size $2M \times N_t$, where $M = 3339$ is the number of patches used to discretize the fault, and N_t is the number of observed epochs from 2007/01/01 up to the time t at which the analysis is conducted. For each patch we have access to the slip potency along both strike and dip, but, since we are studying a subduction zone, we decide to use only the along-dip information because it is one order of magnitude larger and provides a higher signal-to-noise ratio. The geodetic input for our analyses is collected into the matrix P of size $M \times N_t$.

S1.2 Seismic data

We use two tremor catalogs. The first one spans the time period ranging from 2005/01/09 to 2014/12/30 [8] (catalog #1). The second one is the Pacific Northwest Seismic Network (PNSN, https://pnsn.org) tremor catalog that starts on 2009/08/06 and is daily updated [9, 10]. The PNSN catalog is in fact made of two catalogs. With the implementation of an updated detection algorithm capable of providing also estimates of the tremor magnitude, all the seismic waveforms have been reprocessed by [9] starting from 2017-01-01. Such an algorithm is still used today to update the catalog. According to [9], when processing waveforms with both algorithms, the new procedure produced 55% more detections than the old one. When downloading data from the PNSN portal, only the new version is available starting from 2017/01/01. So, we have

a first PNSN catalog pre-2017 (catalog #2) and a second PNSN catalog post-2017 (catalog #3).

Since the magnitude is not provided for all the events, we cannot use the moment rate (or slip potency rate). From the study of post-seismic sequences, it is well known that the cumulative number of aftershocks after a mainshock relaxes over time like the afterslip, which is aseismic slip [11, 12]. It thus seems reasonable to use the number of tremors in one day as a proxy for the slip rate.

We handle the difference in detection capabilities of the three catalogs as follows. First, we reduce each catalog i to a tremors rate spatio-temporal matrix R_i, with the same number of spatial features as the number of patches M, and number of time-stamps equal to the total number of days spanned by the catalog. We merge the three catalogs and use catalog #1 until 2009/08/06, corresponding to the first date for which catalog #2 is available. We adjust the tremors rate R_i multiplying it by a factor γ_i. This factor is equal to 1 for catalog #3, which is the most recent and complete and is thus used as a reference. A direct comparison of the two PNSN catalogs shows no differences in epicentral density [9], so it seems appropriate to simply use a factor of $\gamma_2 = 1.55$ to account for the 55% extra detections of the new catalog. The factor γ_1 is estimated comparing the tremor activities of the catalogs #1 and #2 for the period where both are available. We find the patches and times for which both catalogs have detections and calculate the ratio between the number of events of the catalog #2 and the number of events of the catalog #1. This allows us to refer catalog #1 to catalog #2. We then multiply this ratio by $\gamma_2 = 1.55$ to refer catalog #1 to the reference catalog #3. We obtain a value of $\gamma_1 = 5.7$. We finally multiply the tremors rate (which we assumed to be proportional to the slip rate) by the area over which the tremors occurred to get a quantity proportional to the slip potency rate. We collect these values in a matrix R of size $M \times N_t$, and for brevity we refer to it as tremors rate even if it has been multiplied by an area.

From Figures 1c, 1e, and 1g we see that the catalog #1 does not have a detection capability comparable to the other catalogs. This may limit our capabilities of finding good seismo-geodetic analogs (see Section S4.3) for the period spanned by catalog #1. A uniformly derived high-quality catalog would certainly be beneficial.

S2 Automatic SSEs catalog

To identify the most active segments of the Cascadia subduction, we implement an automatic SSEs detection algorithm to build an SSE catalog. From this catalog, we evaluate the moment released by each patch during an SSE, and thus the total moment released over all experienced SSEs (Figure 1a).

The procedure goes as follows. We use three parameters to define an active patch: two time-windows w and d, and an activation threshold $\Delta P_{\text{threshold}}$. At a given time index n, we define a patch j as active if the average in the window w before n is significantly lower than the average in the window w after a time d. In practice, given the vector $\mathbf{p}_{jn} = [P_{j\ n-w+1}, \dots, P_{jn}]$ we calculate its mean $\mu_j^{(1)}(n)$ and standard deviation $\sigma_j^{(1)}(n)$, where the superscript (1) indicates that these quantities refer to the first window w, the subscript j indicates the patch of interest, and n is the time index of reference. We calculate the same quantities for the vector $\mathbf{p}_{j\ n+d+w} = [P_{j\ n+d+1}, \dots, P_{j\ n+d+w}]$, and call them $\mu_j^{(2)}(n)$ and $\sigma_j^{(2)}(n)$. If $\mu_j^{(2)}(n) - 3\sigma_j^{(2)}(n) > \mu_j^{(1)}(n) + 3\sigma_j^{(1)}(n)$, the patch is active at the time index n. This provides a Boolean spatio-temporal matrix A of active patches. We then create a graph to connect adjacent patches and use it to define SSEs. If a patch becomes active at the time index n, we open an SSE instance that collects all patches that are active at that time and that are adjacent to each other. If any of these adjacent patches was already active, this is the continuation of an ongoing SSE. If none of the adjacent patches was active, this is a marked as a new SSE. At a given time index, we can have multiple SSEs active if they are disjoint. If there are common patches between an SSE

at time $n+1$ and an SSE at time n, we keep the SSE active, otherwise we flag it as terminated. This procedure so far provides a list of potential SSEs and gives tentative start and end time indices for each patch j in the SSE i. We indicate them with $\tilde{n}_j^{(i)\ \mathrm{start}}$ and $\tilde{n}_j^{(i)\ \mathrm{end}}$, respectively. We further introduce a threshold criterion because we may get several false detections. If during the period marked as active at least one patch of those belonging to the SSE experienced a maximum variation in slip potency larger than or equal to $\Delta P_{\mathrm{threshold}} = 5 \times 10^6$ m^3 the SSE is kept, otherwise the SSE is discarded. This threshold corresponds to a magnitude of ≈ 5.4 associated with a single patch and allows us to remove spurious or very small and likely noisy events. To better evaluate the start of the event, for each active patch we search for the minimum of the slip potency in the window $\left[\tilde{n}_j^{(i)\ \mathrm{start}} - w + 1, \tilde{n}_j^{(i)\ \mathrm{start}}\right]$. For the end of the event, we pick the time where the slip potency is maximum in the window $\left[\tilde{n}_j^{(i)\ \mathrm{end}}, \tilde{n}_j^{(i)\ \mathrm{end}} + d + w\right]$. We now have a collection of proposed SSEs. To account for the possible coalescence of SSEs, we merge two SSEs if they share at least one patch at a given time for which they are active.

The whole procedure is repeated "backward" in time. In fact, the active times in the matrix A refer to the end of the first w window, and this may introduce a bias in the start and end times. We thus repeat the procedure, but we flip the time series left-right (to move backward in time) and up-down (so that we can still use the criterion $\mu_j^{(2)}(n) - 3\sigma_j^{(2)}(n) > \mu_j^{(1)}(n) + 3\sigma_j^{(1)}(n)$ to determine the significance in the slip potency difference between two time windows w).

We finally combine the two lists of SSEs obtained with the forward and backward analyses. In this step, we take all the events that are uniquely in the forward and backward catalogs, plus we merge all the events that are shared between the two catalogs.

Figure 1 shows the cumulative moment released by a given patch when summing up the contributions from all the SSEs to which it participated between 2007/01/01

and the first available date in the prospective experiment, namely 2024/08/01. This allows us to get a segmentation for further analyses.

S3 Physical intuition

The fault portion experiencing SSEs shows a clear along-strike segmentation, with a Northern segment (between 47°N and 49°N) slipping more frequently than the central segment (between 44°N and 47°N) [1, 13, 14]. This difference in returning period may be due to the higher loading rate in the Northern portion and to the geometrical configuration of the megathrust, with a clear change in strike at about 47°N. Despite the lower convergence rate, the Southern segment (between 41°N and 44°N) is characterized by more frequent events, but they are smaller and close to the noise level, possibly because frictional properties of the fault interface do not allow high concentration of stresses along this portion of the fault. We further notice that SSEs occur at a depth range of approximately 30-45 km [15]. These observations lead us to the segmentation proposed in Figure 1. See Section S2 for more details about the automatic detection of SSEs and the calculation of the total slip reported in Figure 1.

As a first approximation, we can imagine that each slipping segment is a spring-slider, connected to the other sliders and loaded by the long-term tectonic motion. Concatenated spring-sliders form a so-called Burridge-Knopoff (BK) model [16]. In the simplest case, with a simple velocity weakening friction law [17], the variables needed to fully characterize the state of the system are the slip with respect to the steady loading and the slip velocity of each block. We can multiply the slip and slip velocity by the corresponding slipping area to get the slip potency and slip potency rate [3], which are directly proportional to the seismic moment and moment rate in the case of constant shear modulus.

We do have the slip potency, but unfortunately, we do not have direct access to the slip potency rate. The slip potency derived from geodesy is too noisy to take

a reliable time derivative, and causal filtering would introduce time delays in the signal, detrimental for real-time applications. We exploit the fact that the cumulative number of events often correlates with the observed geodetic deformation [11, 12] (see also Section S1.2), and take the tremors rate as a proxy for the slip rate. We then multiply the tremors rate by the area over which the tremors occurred to get a quantity proportional to the slip potency rate.

[17] showed that a system made of two sliders coupled with a spring and governed by a velocity weakening friction law can undergo chaotic behavior, and hints of chaos have been detected for the Cascadia SSEs system [2]. The simple spring-slider model is to seismology as the Lorenz63 model is to atmospheric science [18]. And as natural occurring analogs can be used in atmospheric science to make weather forecasts [19] and study the characteristic patterns associated with extreme events [20], we start having a sufficient number of SSE cycles to apply similar methods to the study of fault frictional failure. Naturally occurring analogs are past states that are similar to the current state of the system, and in our case the state of the system is determined by the slip potency and the proxy of the slip potency rate derived from the tremors rate.

S4 Forecasting models

S4.1 Deterministic forecasting models

- **Persistence**: The future is equal to the last observed value, i.e., $\hat{P}_j^{(t)}(h) = P_{jN_t}^{(t)}$ and $\Delta\hat{M}_{0\ jt}(h) = 0$.
- **Expectance**: We collect all time windows of length h in the past observations and we take their average to get the expected evolution of the next time window of length h. This gives a value around 0 as expected, since we are using detrended data. This can be seen as a climatological model in atmospheric science, where the expected value is the average of past observations. Since we do not have a well defined period or season, we simply take the expected value of past observations.

- **Persistent rate**: The future is obtained as an extrapolation of the best linear fit performed over the past 7 days, with the idea of trying to capture the onset of a rupture: $\hat{P}_j^{(t)}(h) = P_{jN_t}^{(t)} + h\dot{P}_{j\ N_t-7:N_t}^{(t)}$ where $\dot{P}_{j\ N_t-7:N_t}^{(t)}$ indicates the slope of the best linear fit for patch j in the time window $[N_t - 7, N_t]$.
- **Auto-Regressive (AR)**: We exploit the fact that the slip potency is obtained via an independent component (IC) analysis and fit the best AR model to the inverted ICs. The optimal order of the AR model is automatically selected via the corrected Akaike Information Criterion, and the maximum order is set to 21, i.e. we use maximum the past 3 weeks of data. We use the Julia implementation in the package StateSpaceModels.jl [21].

S4.2 Probabilistic forecasting model

We implement a Brownian Passage Time (BPT) model [22]. It is derived from the Brownian oscillator: a 1-dimensional stochastic differential equation with constant loading rate perturbed by a Wiener process. When the state of the system (in this case representative of the stress on the fault) hits a fixed failure value, the state drops to a fixed ground level. With no perturbations, the state is represented by a periodic saw-tooth pattern. The higher the perturbation, the higher the aperiodicity, typically measured via the coefficient of variation α. This is defined as the ratio between the standard deviation (σ_{BPT}) and the average (μ_{BPT}) of the recurrence time $T_{\mathrm{recurrence}}$. The recurrence time is defined as the time elapsed from a drop in the state (i.e., an event) to the next. For every segment, we define an occurrence of an event as a moment in time for which in the next h days the segment released a magnitude larger than $\tilde{M}_w$. Once an event time is detected, the search for the next event skips the following $w = 90$ days, meaning that we accept only recurrence times larger than w. This seems a reasonable assumption, given that the returning time of SSEs in Cascadia has been previously identified between 8 and 22 months [14], and it allows us to keep just the onset of a failure.

For every day t for which a solution is available, we estimate the recurrence time for each segment for a set of threshold magnitudes $\tilde{M}_w$ ranging from 6.0 to 6.5, equally spaced every 0.1 points of magnitude. This means that, with the new information coming in at time t, we reevaluate the recurrence time and adjust the corresponding mean and coefficient of variation. We finally calculate the elapsed time since the last event larger than $\tilde{M}_w$ and we refer to it with the symbol τ_{BPT}.

The cumulative distribution function of the inverse Gaussian distribution $f(x; \mu_{\mathrm{BPT}}, \lambda_{\mathrm{BPT}})$ with mean μ_{BPT} and shape parameter $\lambda_{\mathrm{BPT}} = \mu_{\mathrm{BPT}}/\alpha^2$ gives the probability that failure will have occurred by the time τ_{BPT}:

$$\mathrm{Prob}(T_{\mathrm{failure}} \leq \tau_{\mathrm{BPT}}) = F(\tau_{\mathrm{BPT}}) = \int_0^{\tau_{\mathrm{BPT}}} f(x; \mu_{\mathrm{BPT}}, \lambda_{\mathrm{BPT}}) \mathrm{d}x \tag{S1}$$

We can use the information that failure did not occur until now, i.e. in the time τ_{BPT} after the last event, to estimate the conditional probability of having a failure in the next h time span:

$$\mathrm{Prob}(T_{\mathrm{failure}} \leq \tau_{\mathrm{BPT}} + h | T_{\mathrm{failure}} > \tau_{\mathrm{BPT}}) = \frac{F(\tau_{\mathrm{BPT}} + h) - F(\tau_{\mathrm{BPT}})}{1 - F(\tau_{\mathrm{BPT}})} \tag{S2}$$

Since we have μ_{BPT}, λ_{BPT}, τ_{BPT}, and h, we can calculate this probability, which will constitute the baseline for our probabilistic forecast assessment.

S4.3 Naturally occurring analogs (NOA) forecasting models

To define naturally occurring analogs we need to declare which observables we use to characterize the state of the system. Inspired by the ideas delineated in the Section S3, we test four different cases:

- **Global geodesy (abbreviation: gl g)**: We search for analogs of P over the whole fault, with similar states (i.e., analogs) defined as those points during the past such that their Euclidean distance from the last column of P is in the bottom 1%.

- **Global seismo-geodesy (abbreviation: gl sg)**: As for the global geodesy case, but now we search for small distances with respect to the vector made of both the normalized slip potency and the normalized tremor rate times area at time N_t. For each dataset, we use a min-max normalization approach for each patch.
- **Segmented geodesy (abbreviation: seg g)**: Given the 30 segments (Figure 1 and Section S3), for each segment i we search for analogs of $\left[P_{\mathcal{A}_i^{-1}\ N_t}, P_{\mathcal{A}_i\ N_t}, P_{\mathcal{A}_i^{+1}\ N_t}\right]^T$, where $\mathcal{A}_i^{-1}$ and $\mathcal{A}_i^{+1}$ indicate the areas of the along-strike neighbor segments. If the segment i is at the extreme North or South, i.e. it does have only one neighbor along-strike, we reduce the vector to 2-dimension.
- **Segmented seismo-geodesy (abbreviation: seg sg)**: As for the segmented geodesy case, but we search for analogs of $\left[\tilde{P}_{\mathcal{A}_i^{-1}\ N_t}, \tilde{P}_{\mathcal{A}_i\ N_t}, \tilde{P}_{\mathcal{A}_i^{+1}\ N_t}, \tilde{R}_{\mathcal{A}_i^{-1}\ N_t}, \tilde{R}_{\mathcal{A}_i\ N_t}, \tilde{R}_{\mathcal{A}_i^{+1}\ N_t}\right]^T$, where $\tilde{P}$ and $\tilde{R}$ indicate the normalized slip potency and tremors rate times area. Time series associated with each segment are individually normalized using a min-max normalization.

The only hyper-parameter involved is the number of analogs to retain. We set it to 1% of N_t, a value already successfully used in various geophysical contexts when searching for analogs in daily data to study extreme events with recurrence times of similar duration as the ones considered here [2, 23]. To avoid using highly correlated recent states, we automatically select a Theiler window via the first zero of the auto-correlation function [24]. Compared to an AR approach, we have the advantage that we can look as far back as data allows, so that we have recent information via the present state and past information via the analogs at a sufficient distance back in time to avoid recent high correlations.

S5 Evaluation metrics

For deterministic forecasts, we use the Mean Absolute Error (MAE) between $\Delta\hat{M}_{0\ \mathcal{A}t}(h)$ and $\Delta M_{0\ \mathcal{A}t}(h)$, with $t = 1, \ldots, T-h$. We also split the times $t =$

$1, \ldots, T-h$ into active and inactive periods, to evaluate the performance separately. An active time is defined as a day such that $\Delta M_{0\ \mathcal{A}}(h) > \tilde{M}_0$, where $\tilde{M}_0$ is a threshold moment corresponding to a desired threshold magnitude $\tilde{M}_w$. This allows us to also evaluate the confusion matrix and associated quantities like precision, recall, accuracy, and F1-score. For a given segment, the confusion matrix depends on the decided moment threshold $\tilde{M}_0$ and on the forecasting horizon h. A day is a true positive if both $\Delta M_{0\ \mathcal{A}}(h) > \tilde{M}_0$ and $\Delta \hat{M}_{0\ \mathcal{A}}(h) > \tilde{M}_0$, a true negative if $\Delta M_{0\ \mathcal{A}}(h) \leq \tilde{M}_0$ and $\Delta \hat{M}_{0\ \mathcal{A}}(h) \leq \tilde{M}_0$, a false positive if $\Delta M_{0\ \mathcal{A}}(h) \leq \tilde{M}_0$ and $\Delta \hat{M}_{0\ \mathcal{A}}(h) > \tilde{M}_0$, and a false negative if $\Delta M_{0\ \mathcal{A}}(h) > \tilde{M}_0$ and $\Delta \hat{M}_{0\ \mathcal{A}}(h) \leq \tilde{M}_0$. We recognize that there is a severe class imbalance, with many inactive times and few active times. This may lead to artificially high accuracy values. For example, for the Northern segment and $\tilde{M}_w = 6.3$ we find an accuracy larger than 90% for all tested forecasting horizons and for all models except the persistent rate one. This shows that even the persistence model, which gives no alarms at all, can get a very high accuracy, simply because of the large proportion of inactive times.

Furthermore, according to this definition of active and inactive times, we will have multiple days in a row labelled as active, even if the SSE is still the same and is unraveling over several weeks. This may lead to artificially low recall values. Taking once again the Northern segment and $\tilde{M}_w = 6.3$, we find that the expectation model is the one with the highest recall, with a maximum value of 32% for $h = 21$ days. Among the non-trivial models, the segmented seismo-geodesy one obtains the highest recall, with values ranging between 6.2% to 21%. We realize that these small values are artificially low because of our definition of active times. Since we have only two SSEs in the tested period, remembering that the recall is given by the ratio between the number of retrieved events over the total number of events, we should expect only recall values of 0%, 50% or 100%. Having a value of 21% does not mean that we identify only about 1 SSE every 5. In fact, both events have been correctly identified at all

forecasting horizons, as shown in Figure 4. But not all active times have been correctly identified (only about one in five active times in the best case). A more appropriate estimation of the goodness of a model can be obtained with probabilistic forecasts, and not just binary evaluations of the presence or absence of an event. Since we also have an ensemble forecast via the analogs approach, we can estimate the probability of having a certain slip potency in the future (see Movie S1), or the probability of having a magnitude larger than a certain desired alarm threshold in the next h days (Figure 4). To evaluate the goodness of a probabilistic forecast, we use the Brier score for various levels of alarm magnitude threshold.

We evaluate the skill score of every model against a baseline model. We define the skill score (SS) as:

$$\mathrm{SS}_{\mathrm{metric}}(\mathrm{model}, \mathrm{ref}) = 1 - \frac{\mathrm{metric}(\mathrm{model})}{\mathrm{metric}(\mathrm{ref})} \tag{S3}$$

where metric is MAE for deterministic models and Brier for probabilistic models, model is one of the forecasting methods listed before (see Section S4), and ref is the specific reference model to compare the tested model against.

S6 Figures

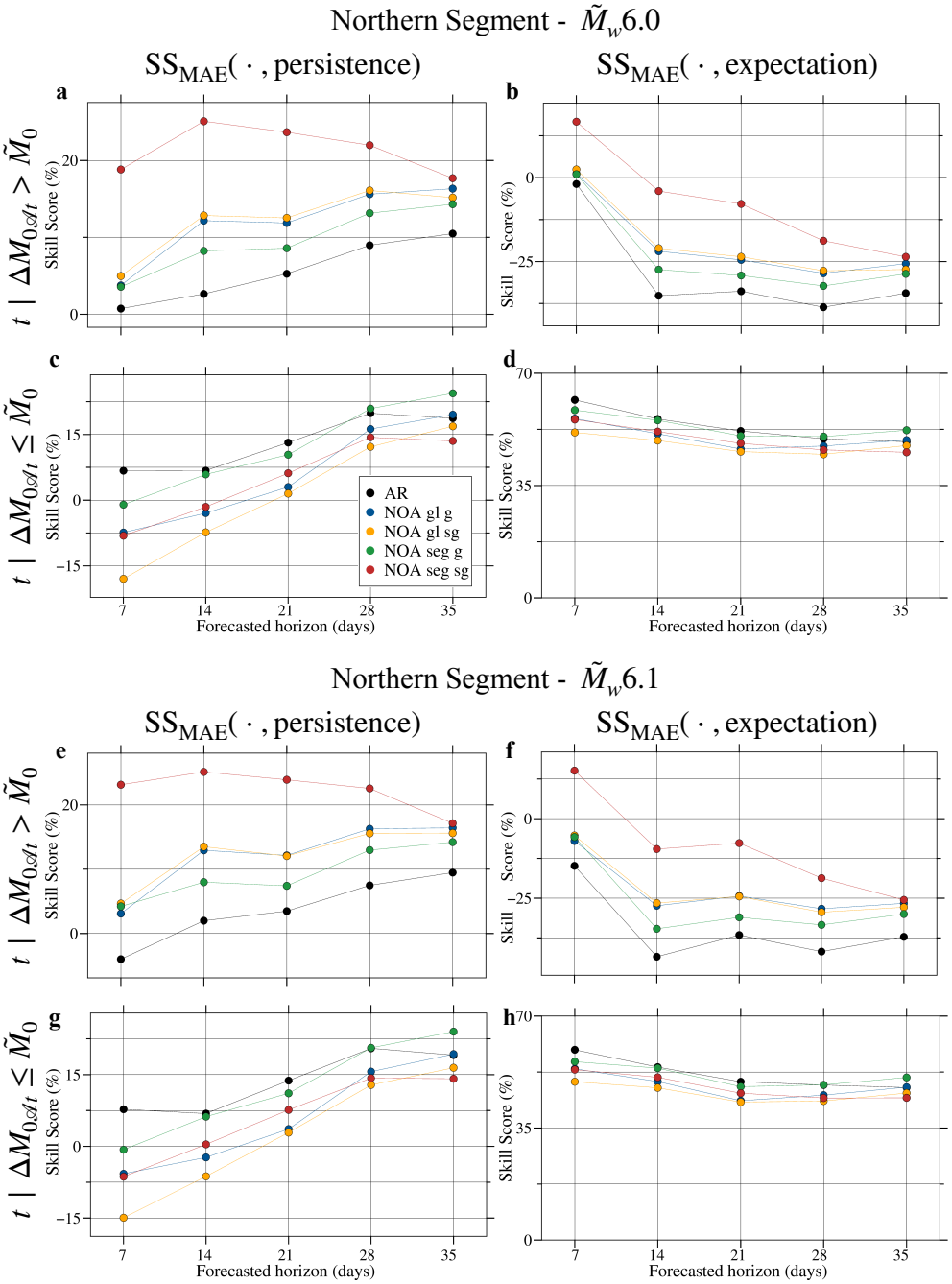

Fig. S1 As Figure 3 for the active and inactive times, but for $\tilde{M}_w = 6.0$ (panels a-d) and $\tilde{M}_w = 6.1$ (panels e-h).

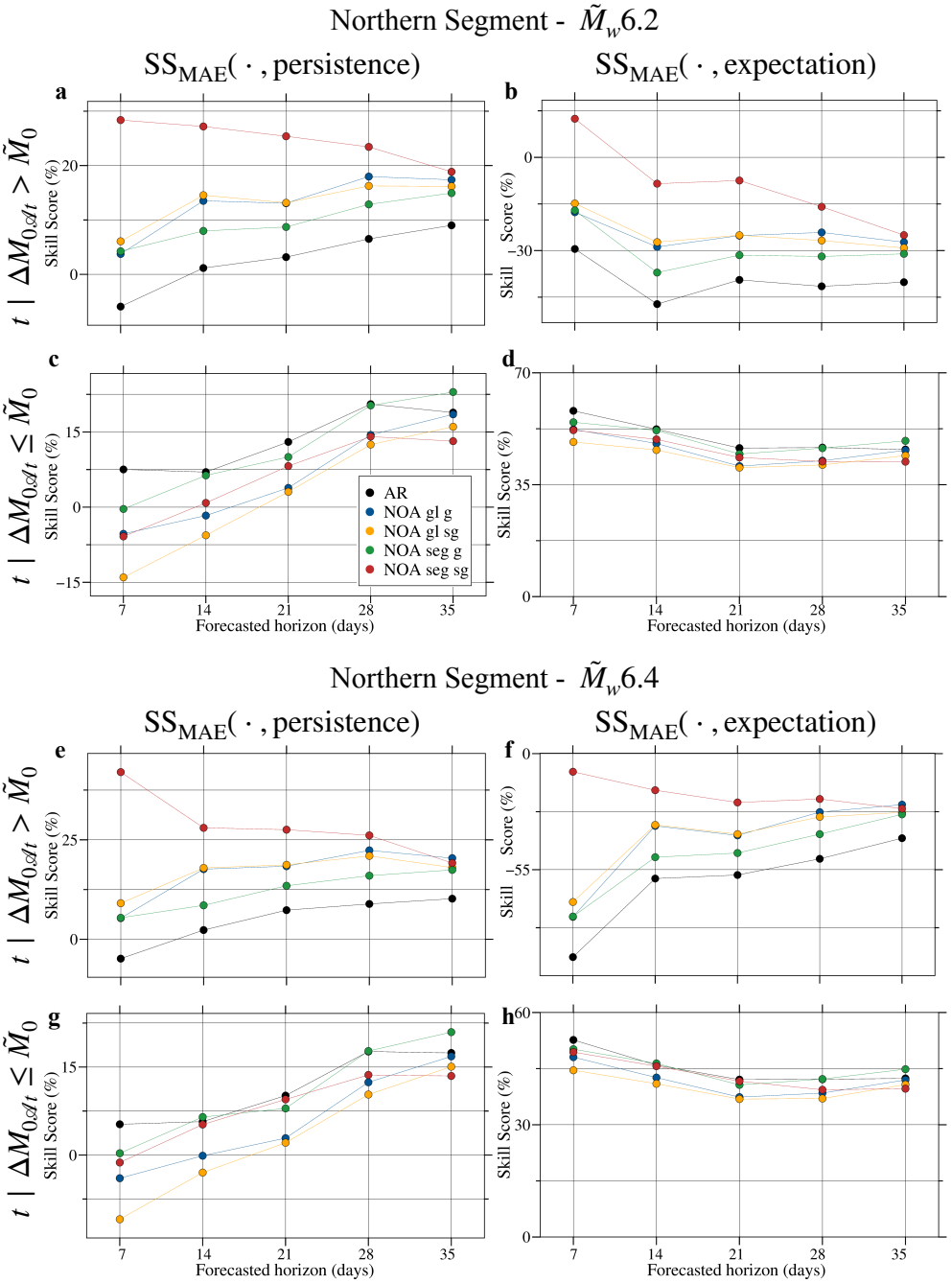

Fig. S2 As Figure 3 for the active and inactive times, but for $\tilde{M}_w = 6.2$ (panels a-d) and $\tilde{M}_w = 6.4$ (panels e-h).

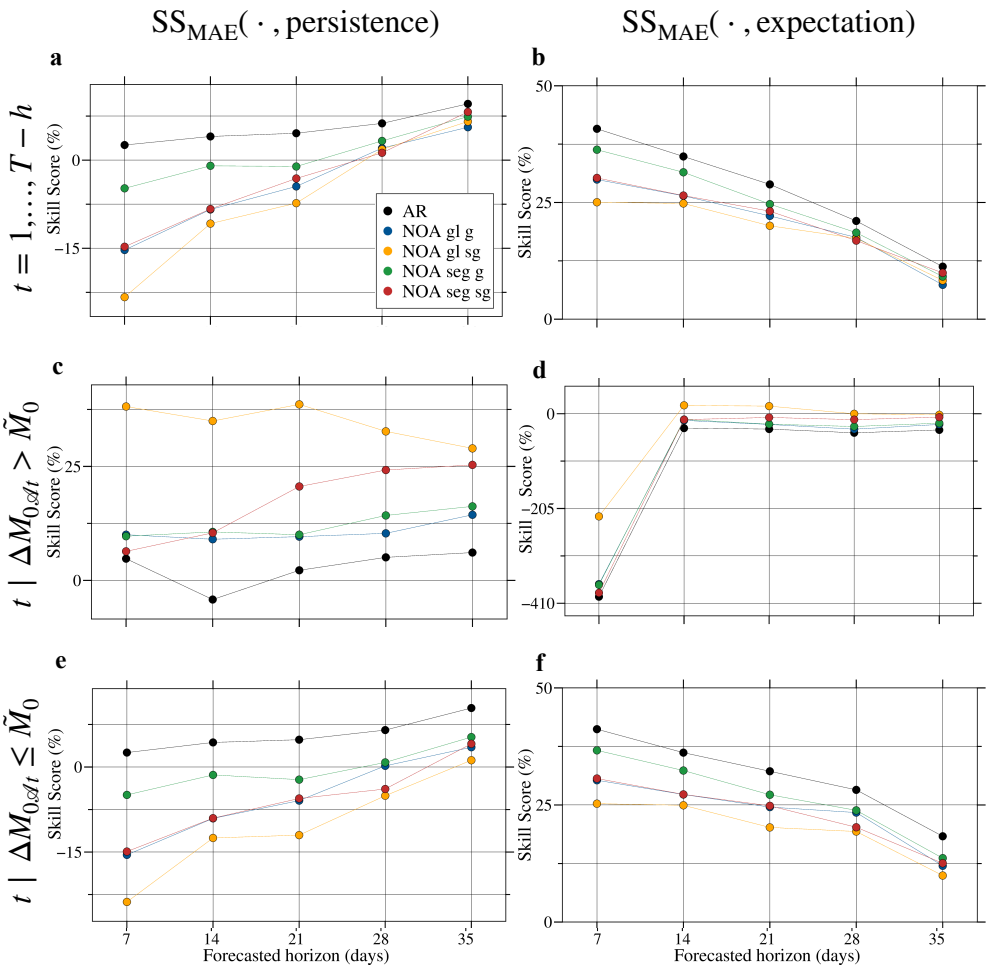

Fig. S3 As Figure 3, but for the central segment and for $\tilde{M}_w = 6.2$ because for $h = 7$ days and $h = 14$ days there were no active days when using $\tilde{M}_w \geq 6.3$.

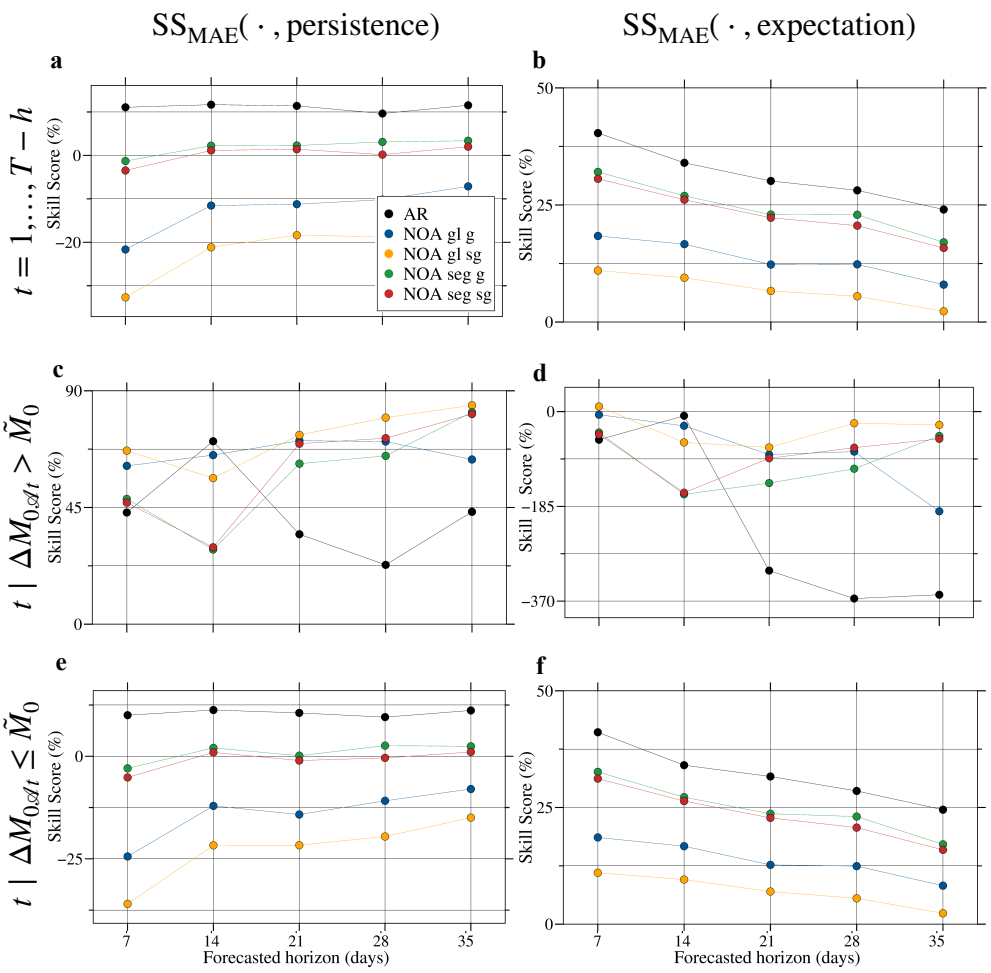

Fig. S4 As Figure 3, but for the Southern segment and with $\tilde{M}_w = 6.0$ because there were no active dates with $\tilde{M}_w > 6.0$ for all tested forecasting horizons but $h = 21$ days.

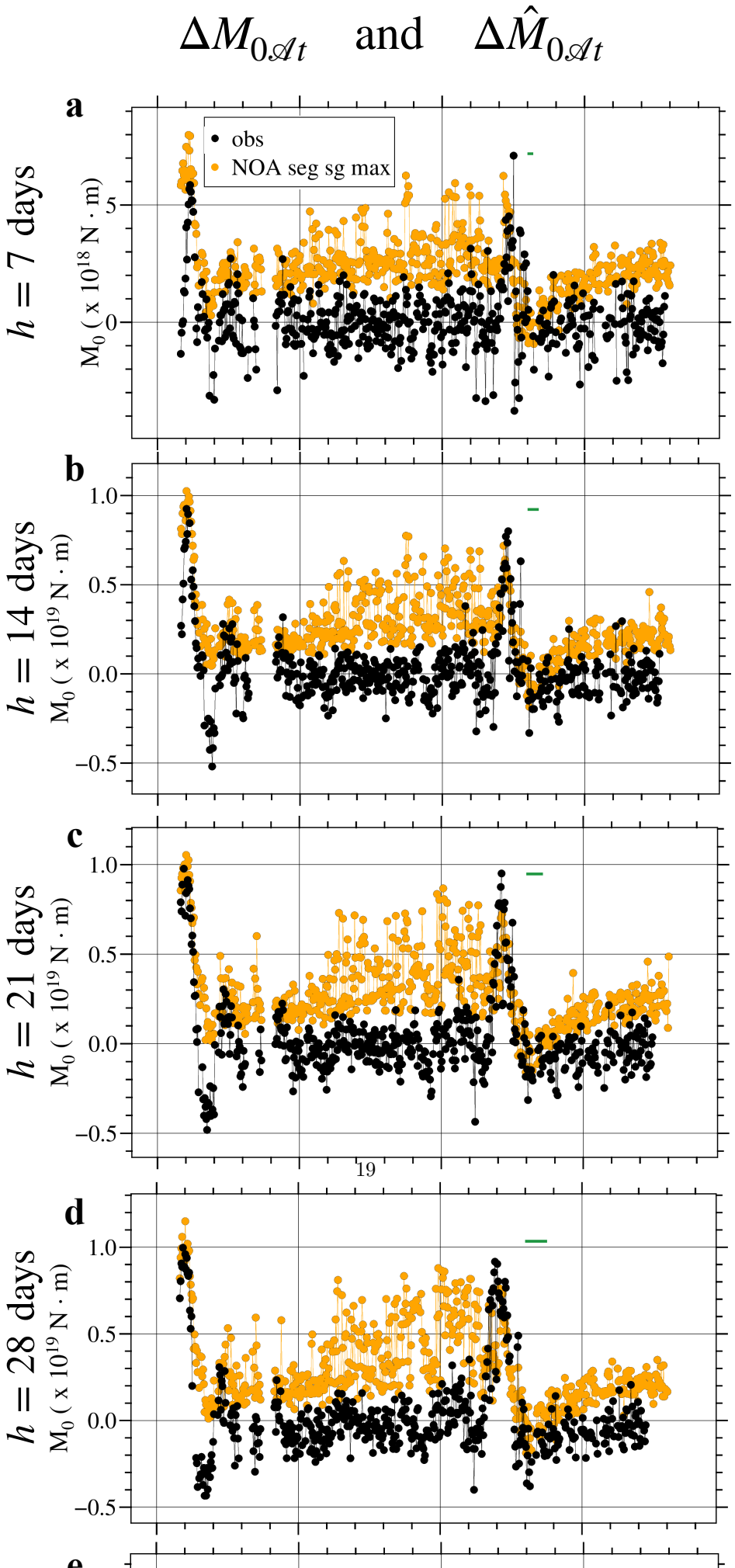
$\Delta M_{0\mathscr{A}t}$ and $\Delta \hat{M}_{0\mathscr{A}t}$
a
b
c
d
obs
NOA seg sg max
h = 7 days
h = 14 days
h = 21 days
h = 28 days
M0 (x 10^18 N · m)
M0 (x 10^19 N · m)
5
0
1.0
0.5
0.0
−0.5

S7 Tables

Table S1 MAE skill score of each model vs. the persistence and expectation models for the Northern segment for various forecasted horizons. Non-negative skill scores are highlighted in bold, and for each forecasted horizon the value of the best performing model is underlined.

Model	Northern segment									
	SS_{MAE}(model, persistence) h (days)					SS_{MAE}(model, expectation) h (days)				
	7	14	21	28	35	7	14	21	28	35
Persistence	-	-	-	-	-	47%	34%	22%	12%	14%
Expectation	-90%	-51%	-28%	-13%	-16%	-	-	-	-	-
Persistent rate	-140%	-140%	-140%	-160%	-210%	-26%	-58%	-90%	-130%	-170%
AR	**4.5**%	**5.0**%	**9.3**%	**15**%	**15**%	**50**%	**37**%	**29**%	**25**%	**27**%
NOA gl g	-3.3%	**3.6**%	**7.3**%	**16**%	**18**%	**46**%	**36**%	**27**%	**26**%	**29**%
NOA gl sg	-9.6%	**1.3**%	**6.8**%	**14**%	**16**%	**42**%	**35**%	**27**%	**24**%	**28**%
NOA seg g	**0.65**%	**6.9**%	**9.5**%	**17**%	**20**%	**48**%	**38**%	**29**%	**27**%	**31**%
NOA seg sg	**1.7**%	**9.9**%	**15**%	**18**%	**15**%	**48**%	**40**%	**33**%	**28**%	**27**%

Table S2 MAE skill score of each model vs. the persistence and expectation models for the Northern segment for various forecasted horizons for active times, defined using $\tilde{M}_w = 6.3$. Non-negative skill scores are highlighted in bold, and for each forecasted horizon the value of the best performing model is underlined.

Model	Northern segment active times (i.e., $t \mid \Delta M_{0\ \mathcal{A}t} > \tilde{M}_0$, with $\tilde{M}_0$ such that $\tilde{M}_w = 6.3$)									
	SS_{MAE}(model, persistence) h (days)					SS_{MAE}(model, expectation) h (days)				
	7	14	21	28	35	7	14	21	28	35
Persistence	-	-	-	-	-	-54%	-66%	-54%	-53%	-56%
Expectation	**35**%	**40**%	**35**%	**35**%	**36**%	-	-	-	-	-
Persistent rate	-46%	-25%	-22%	-25%	-37%	-120%	-110%	-87%	-92%	-110%
AR	-1.7%	**2.0**%	**5.1**%	**7.0**%	**10**%	-57%	-63%	-46%	-43%	-40%
NOA gl g	**8.7**%	**16**%	**15**%	**19**%	**19**%	-41%	-39%	-30%	-24%	-26%
NOA gl sg	**13**%	**17**%	**16**%	**18**%	**18**%	-34%	-38%	-30%	-26%	-28%
NOA seg g	**6.8**%	**8.6**%	**11**%	**14**%	**17**%	-44%	-52%	-37%	-32%	-30%
NOA seg sg	**37**%	**29**%	**26**%	**26**%	**19**%	**2.5**%	-17%	-14%	-14%	-26%

Table S3 MAE skill score of each model vs. the persistence and expectation models for the Northern segment for various forecasted horizons for inactive times, defined using $\tilde{M}_w = 6.3$. Non-negative skill scores are highlighted in bold, and for each forecasted horizon the value of the best performing model is underlined.

Model	Northern segment inactive times (i.e., $t \mid \Delta M_{0\ \mathcal{A}t} \leq \tilde{M}_0$, with $\tilde{M}_0$ such that $\tilde{M}_w = 6.3$) SS_{MAE}(model, persistence) h (days)					SS_{MAE}(model, expectation) h (days)				
	7	14	21	28	35	7	14	21	28	35
Persistence	-	-	-	-	-	53%	47%	37%	31%	31%
Expectation	-110%	-89%	-58%	-44%	-46%	-	-	-	-	-
Persistent rate	-160%	-190%	-200%	-240%	-310%	-20%	-51%	-90%	-130%	-180%
AR	**5.7%**	**6.2%**	**11%**	**19%**	**18%**	**56%**	**50%**	**44%**	**44%**	**43%**
NOA gl g	-5.5%	-1.7%	**3.3%**	**14%**	**17%**	**50%**	**46%**	**39%**	**40%**	**43%**
NOA gl sg	-14%	-5.2%	**2.5%**	**12%**	**15%**	**47%**	**44%**	**38%**	**39%**	**42%**
NOA seg g	-0.49%	**6.2%**	**9.0%**	**19%**	**22%**	**53%**	**50%**	**43%**	**44%**	**46%**
NOA seg sg	-4.7%	**1.9%**	**9.1%**	**13%**	**13%**	**51%**	**48%**	**43%**	**40%**	**41%**

Table S4 Brier skill score of each model vs. the BPT model for the Northern segment for various forecasted horizons for two threshold magnitudes, $\tilde{M}_w = 6.1$ and $\tilde{M}_w = 6.2$. Non-negative skill scores are highlighted in bold, and for each forecasted horizon the value of the best performing model is underlined.

Model	Northern segment SS_{Brier}(model, BPT) for $\tilde{M}_w = 6.1$ h (days)					SS_{Brier}(model, BPT) for $\tilde{M}_w = 6.2$ h (days)				
	7	14	21	28	35	7	14	21	28	35
Persistence	**14%**	**14%**	**18%**	**21%**	**31%**	**4.6%**	**3%**	**2.6%**	-0.7%	**8.6%**
Expectation	-98%	-46%	-2.1%	**5.1%**	**9.4%**	-70%	-28%	-20%	**3.2%**	**2.7%**
Persistent rate	-260%	-240%	-170%	-180%	-180%	-360%	-260%	-240%	-250%	-300%
AR	**14%**	**14%**	**18%**	**23%**	**33%**	**4.6%**	**3%**	**2.6%**	-0.7%	**8.6%**
NOA gl g	**19%**	**31%**	**34%**	**41%**	**44%**	**9.1%**	**19%**	**20%**	**24%**	**26%**
NOA gl sg	**14%**	**28%**	**33%**	**38%**	**42%**	**9.7%**	**18%**	**18%**	**20%**	**22%**
NOA seg g	**20%**	**26%**	**30%**	**40%**	**48%**	**7.9%**	**13%**	**18%**	**20%**	**29%**
NOA seg sg	**34%**	**37%**	**44%**	**46%**	**42%**	**30%**	**31%**	**37%**	**31%**	**23%**

Table S5 As Table S4, but for threshold magnitudes $\tilde{M}_w = 6.3$ and $\tilde{M}_w = 6.4$.

Model	Northern segment SS_{Brier}(model, BPT) for $\tilde{M}_w = 6.3$ h (days)					SS_{Brier}(model, BPT) for $\tilde{M}_w = 6.4$ h (days)				
	7	14	21	28	35	7	14	21	28	35
Persistence	-17%	-42%	-29%	-21%	-25%	-20%	-2.4%	-12%	-11%	-29%
Expectation	-39%	-18%	**5.3%**	**16%**	-1.4%	-160%	**3.3%**	**0.00%**	**10%**	-9.8%
Persistent rate	-460%	-390%	-300%	-270%	-420%	-440%	-200%	-200%	-180%	-320%
AR	-17%	-42%	-29%	-21%	-25%	-20%	-2.4%	-12%	-11%	-29%
NOA gl g	-13%	-22%	-7.4%	**7.7%**	-2.0%	-21%	**8%**	**3.2%**	**13%**	-5.3%
NOA gl sg	-10%	-25%	-11%	**2.0%**	-12%	-21%	**4.6%**	**1.2%**	**7.9%**	-13%
NOA seg g	-15%	-28%	-8.5%	**3.0%**	**1.9%**	-20%	**4.8%**	**4.3%**	**12%**	-1.4%
NOA seg sg	**18%**	**0.75%**	**13%**	**17%**	-9.4%	**3.7%**	**17%**	**20%**	**21%**	-7.4%

Table S6 As Table S1, but for the central segment and with active times defined using $\tilde{M}_w = 6.2$.

Model	Central segment									
	SS_{MAE}(model, persistence) h (days)					SS_{MAE}(model, expectation) h (days)				
	7	14	21	28	35	7	14	21	28	35
Persistence	-	-	-	-	-	**39%**	**32%**	**25%**	**16%**	**1.9%**
Expectation	-65%	-47%	-34%	-19%	-1.9%	-	-	-	-	-
Persistent rate	-110%	-130%	-150%	-170%	-180%	-29%	-54%	-88%	-130%	-170%
AR	**2.6%**	**4.0%**	**4.6%**	**6.2%**	**9.6%**	**41%**	**35%**	**29%**	**21%**	**11%**
NOA gl g	-15%	-8.4%	-4.5%	**2.1%**	**5.6%**	**30%**	**26%**	**22%**	**18%**	**7.4%**
NOA gl sg	-23%	-11%	-7.3%	**1.8%**	**6.6%**	**25%**	**25%**	**20%**	**17%**	**8.3%**
NOA seg g	-4.8%	-0.97%	-1.1%	**3.3%**	**7.4%**	**36%**	**31%**	**25%**	**19%**	**9.1%**
NOA seg sg	-15%	-8.3%	-3.1%	**1.2%**	**8.2%**	**30%**	**26%**	**23%**	**17%**	**9.9%**

Table S7 As Table S2, but for the central segment and with active times defined using $\tilde{M}_w = 6.2$.

Model	Central segment active times (i.e., $t \mid \Delta M_{0\ \mathcal{A}t} > \tilde{M}_0$, with $\tilde{M}_0$ such that $\tilde{M}_w = 6.2$)									
	SS_{MAE}(model, persistence) h (days)					SS_{MAE}(model, expectation) h (days)				
	7	14	21	28	35	7	14	21	28	35
Persistence	-	-	-	-	-	-420%	-26%	-36%	-49%	-44%
Expectation	**81%**	**21%**	**27%**	**33%**	**31%**	-	-	-	-	-
Persistent rate	-74%	-1.5%	-6%	-15%	-20%	-800%	-28%	-44%	-72%	-72%
AR	**4.8%**	-4.2%	**2.2%**	**5.1%**	**6.1%**	-400%	-31%	-33%	-41%	-35%
NOA gl g	**10%**	**9.0%**	**9.6%**	**10%**	**14%**	-370%	-15%	-23%	-34%	-23%
NOA gl sg	**38%**	**35%**	**39%**	**33%**	**29%**	-220%	**18%**	**16%**	-0.23%	-2.3%
NOA seg g	**9.7%**	**11%**	**10%**	**14%**	**16%**	-370%	-13%	-23%	-28%	-21%
NOA seg sg	**6.4%**	**10%**	**21%**	**24%**	**25%**	-390%	-13%	-8.3%	-13%	-7.6%

Table S8 As Table S3, but for the central segment and with inactive times defined using $\tilde{M}_w = 6.2$.

Model	Central segment inactive times (i.e., $t \mid \Delta M_{0\ \mathcal{A}t} \leq \tilde{M}_0$, with $\tilde{M}_0$ such that $\tilde{M}_w = 6.2$)									
	SS_{MAE}(model, persistence) h (days)					SS_{MAE}(model, expectation) h (days)				
	7	14	21	28	35	7	14	21	28	35
Persistence	-	-	-	-	-	**40%**	**33%**	**29%**	**23%**	**8.8%**
Expectation	-66%	-50%	-40%	-30%	-9.7%	-	-	-	-	-
Persistent rate	-110%	-130%	-170%	-200%	-220%	-29%	-55%	-90%	-130%	-190%
AR	**2.5%**	**4.3%**	**4.8%**	**6.5%**	**10%**	**41%**	**36%**	**32%**	**28%**	**18%**
NOA gl g	-16%	-9.1%	-5.9%	**0.21%**	**3.5%**	**30%**	**27%**	**25%**	**23%**	**12%**
NOA gl sg	-24%	-13%	-12%	-5.1%	**1.2%**	**25%**	**25%**	**20%**	**19%**	**9.9%**
NOA seg g	-4.9%	-1.4%	-2.2%	**0.81%**	**5.3%**	**37%**	**32%**	**27%**	**24%**	**14%**
NOA seg sg	-15%	-9.0%	-5.5%	-3.9%	**4.1%**	**31%**	**27%**	**25%**	**20%**	**13%**

Table S9 As Table S1, but for the Southern segment and with active times defined using $\tilde{M}_w = 6.0$.

Model	Southern segment									
	SS_{MAE}(model, persistence)					SS_{MAE}(model, expectation)				
	h (days)					h (days)				
	7	14	21	28	35	7	14	21	28	35
Persistence	-	-	-	-	-	**33%**	**25%**	**21%**	**20%**	**14%**
Expectation	-49%	-34%	-27%	-26%	-16%	-	-	-	-	-
Persistent rate	-98%	-130%	-170%	-220%	-260%	-33%	-69%	-110%	-160%	-210%
AR	**11%**	**12%**	**11%**	**9.6%**	**12%**	**40%**	**34%**	**30%**	**28%**	**24%**
NOA gl g	-22%	-12%	-11%	-10%	-7.1%	**18%**	**17%**	**12%**	**12%**	**8%**
NOA gl sg	-33%	-21%	-18%	-19%	-14%	**11%**	**9.5%**	**6.6%**	**5.5%**	**2.3%**
NOA seg g	-1.3%	**2.2%**	**2.3%**	**3.1%**	**3.4%**	**32%**	**27%**	**23%**	**23%**	**17%**
NOA seg sg	-3.5%	**1.1%**	**1.4%**	**0.18%**	**2.0%**	**31%**	**26%**	**22%**	**21%**	**16%**

Table S10 As Table S2, but for the Southern segment and with active times defined using $\tilde{M}_w = 6.0$.

Model	Southern segment active times (i.e., $t \mid \Delta M_{0\ \mathcal{A}t} > \tilde{M}_0$, with $\tilde{M}_0$ such that $\tilde{M}_w = 6.0$)									
	SS_{MAE}(model, persistence)					SS_{MAE}(model, expectation)				
	h (days)					h (days)				
	7	14	21	28	35	7	14	21	28	35
Persistence	-	-	-	-	-	-170%	-270%	-530%	-500%	-710%
Expectation	**63%**	**73%**	**84%**	**83%**	**88%**	-	-	-	-	-
Persistent rate	-68%	-66%	-120%	-59%	-33%	-360%	-510%	-1300%	-860%	-970%
AR	**43%**	**71%**	**35%**	**23%**	**43%**	-55%	-8.2%	-310%	-360%	-360%
NOA gl g	**61%**	**65%**	**71%**	**70%**	**64%**	-6.0%	-28%	-84%	-78%	-190%
NOA gl sg	**67%**	**56%**	**73%**	**80%**	**84%**	**9.9%**	-60%	-70%	-23%	-26%
NOA seg g	**48%**	**29%**	**62%**	**65%**	**82%**	-41%	-160%	-140%	-110%	-48%
NOA seg sg	**47%**	**30%**	**70%**	**72%**	**81%**	-45%	-160%	-91%	-70%	-53%

Table S11 As Table S3, but for the Southern segment and with inactive times defined using $\tilde{M}_w = 6.0$.

Model	Southern segment inactive times (i.e., $t \mid \Delta M_{0\ \mathcal{A}t} \leq \tilde{M}_0$, with $\tilde{M}_0$ such that $\tilde{M}_w = 6.0$)									
	SS_{MAE}(model, persistence)					SS_{MAE}(model, expectation)				
	h (days)					h (days)				
	7	14	21	28	35	7	14	21	28	35
Persistence	-	-	-	-	-	**35%**	**26%**	**24%**	**21%**	**15%**
Expectation	-53%	-35%	-31%	-27%	-18%	-	-	-	-	-
Persistent rate	-99%	-130%	-170%	-230%	-270%	-30%	-69%	-110%	-160%	-210%
AR	**10%**	**11%**	**11%**	**9.5%**	**11%**	**41%**	**34%**	**32%**	**29%**	**25%**
NOA gl g	-24%	-12%	-14%	-11%	-8.0%	**19%**	**17%**	**13%**	**12%**	**8.2%**
NOA gl sg	-36%	-22%	-22%	-20%	-15%	**11%**	**9.6%**	**7.0%**	**5.5%**	**2.3%**
NOA seg g	-3.0%	**2.0%**	**0.13%**	**2.6%**	**2.4%**	**33%**	**27%**	**24%**	**23%**	**17%**
NOA seg sg	-5.2%	**0.94%**	-1.0%	0.41%	**1.0%**	**31%**	**26%**	**23%**	**21%**	**16%**

S8 Movie

Observed vs. forecasted slip potency in the next $h = 21$ days for the Northern segment. The blue dot indicates the last observed value (labelled as "present"). The black dots show the observed future evolution of the slip potency as per the solution retrieved 21 days in the future. Green dots show the weighted mean of the analog-based segmented seismo-geodesy model. The green lines indicate the evolution of all analogs used (1% of N_t). The hot colormap indicates the probability to have a certain value according to the evolution of the analogs used.

References

[1] Gualandi, A.: Near real-time cascadia slow slip events. Geophysical Journal International **242**, 1–14 (2025)

[2] Gualandi, A., Avouac, J.-P., Michel, S., Faranda, D.: The predictable chaos of slow earthquakes. Sci. Adv. **6**(27) (2020) https://doi.org/10.1126/sciadv.aaz5548

[3] Anghel, M., Ben-Zion, Y., Rico-Martinez, R.: Dynamical system analysis and forecasting of deformation produced by an earthquake fault. Pure appl. geophys. **161**, 2023–2051 (2004)

[4] Hasterok, D., Halpin, J., Collins, A., Hand, M., Kreemer, C., Gard, M., Glorie, S.: New maps of global geological provinces and tectonic plates. Earth-Sci. Rev. **231** (2022)

[5] Nikkhoo, M., Walter, T.: Triangular dislocation: an analytical, artefact-free solution. Geophys. J. Int. **201**, 1119–1141 (2015)

[6] Árnadottir, T., Segall, P.: The 1989 loma prieta earthquake imaged from inversion of geodetic data. J. Geophys. Res. **99**, 21835–21855 (1994)

[7] Freymueller, J., King, N.E., Segall, P.: The co-seismic slip distribution of the landers earthquake. Bull. seism. Soc. Am. **84**, 646–659 (1994)

[8] Ide, S.: Variety and spatial heterogeneity of tectonic tremor worldwide. Journal of Geophysical Research: Solid Earth **117** (2012)

[9] Wech, A.G.: Cataloging tectonic tremor energy radiation in the cascadia subduction zone. Journal of Geophysical Research: Solid Earth **126** (2021)

[10] Wech, A.G.: Interactive tremor monitoring. Seismological Research Letters **81**, 664–669 (2010)

[11] Perfettini, H., Avouac, J.-P.: Postseismic relaxation driven by brittle creep: A possible mechanism to reconcile geodetic measurements and the decay rate of aftershocks, application to the chi-chi earthquake, taiwan. J. Geophys. Res. **109**(B02304) (2004) https://doi.org/10.1029/2003JB002488

[12] Gualandi, A., Liu, Z., Rollins, C.: Post-large earthquake seismic activities mediated by aseismic deformation processes. Earth and Planetary Science Letters **530**(115870) (2020) https://doi.org/10.1016/j.epsl.2019.115870

[13] Michel, S., Gualandi, A., Avouac, J.-P.: Interseismic coupling and slow slip events on the cascadia megathrust. PAGEOPH **176**, 3867–3891 (2019) https://doi.org/10.1007/s00024-018-1991-x

[14] Bartlow, N.: A long-term view of episodic tremor and slip in cascadia. Geophysical Research Letters **47**(e2019GL085303) (2020) https://doi.org/10.1029/2019GL085303

[15] Behr, W.M., Bürgmann, R.: What's down there? the structures, materials and environment of deep-seated slow slip and tremor. Phil. Trans. R. Soc. A **379**

(2021)

[16] Burridge, R., Knopoff, L.: Model and theoretical seismicity. Bulletin of the Seismological Society of America **57**, 341–371 (1967)

[17] Huang, J., Turcotte, D.L.: Evidence for chaotic fault inter- actions in the seismicity of the san andreas fault and nankai trough. Nature **348**, 234–236 (1990)

[18] Ghil, M.: A century of nonlinearity in the geosciences. Earth and Space Science **6**, 1007–1042 (2019)

[19] Lorenz, E.N.: Atmospheric predictability as revealed by naturally occurring analogs. Journal of the Atmospheric Sciences **26**, 636–646 (1969)

[20] Dong, C., Noyelle, R., Messori, G., Gualandi, A., Fery, L., Yiou, P., Vrac, M., D'Andrea, F., Camargo, S.J., Coppola, E., Balsamo, G., Chen, C., Faranda, D., Mengaldo, G.: Indo-pacific regional extremes aggravated by changes in tropical weather patterns. Nature Geoscience **17**, 979–986 (2014)

[21] Saavedra, R., Bodin, G., Souto, M.: Statespacemodels.jl: a julia package for time-series analysis in a state-space framework. arXiv (2020) https://doi.org/10.48550/arXiv.1908.01757

[22] Matthews, M.V., Ellsworth, W.L., Reasenberg, P.A.: A brownian model for recurrent earthquakes. Bulletin of the Seismological Society of America **92**(6), 2233–2250 (2002)

[23] Faranda, D., Messori, G., Yiou, P.: Dynamical proxies of north atlantic predictability and extremes. Scientific Reports **7**(41278) (2017) https://doi.org/10.1038/srep41278

[24] Theiler, J.: Spurious dimension from correlation algorithms applied to limited

time-series data. Physical Review A **34**, 2427–2432 (1986)